Nanoscale Advances

ROYAL SOCIETY OF CHEMISTRY

COMMUNICATION

View Article Online
View Journal

Cite this: DOI: 10.1039/d5na01116g

Received 3rd December 2025
Accepted 11th April 2026

DOI: 10.1039/d5na01116g

rsc.li/nanoscale-advances

A nanoporous $Ni(OH)_2$ interlinked Co_3O_4 heterojunction: a novel approach to chromium(VI) detection

Gitashree Darabdhara,[a] Manash J. Baruah,[b] Eramoni Saikia,[c] Shivanee Borpatra Gohain,[d] Rajarshi Bayan,[e] Rahul Kemprai,[f] Dipankoj Gogoi,[g] Young-Bin Park,[h] Biraj Das *[c] and Mukesh Sharma *[f]

The present study broadly explores the synthesis, structural characteristics, and electrochemical performance of a nanoporous $Ni(OH)_2$/Co_3O_4 heterojunction engineered for efficient enzymatic sensing of hexavalent chromium Cr(VI). The synthesized heterostructure consists of a porous $Ni(OH)_2$/Co_3O_4 matrix (nanopores, with dimensions approximately ranging from 6 to 10 nm) intimately coupled with evenly dispersed Co_3O_4 nanocrystals, forming a well-integrated interface that enables strong synergistic redox coupling and rapid electron transport across the junction. The nanoporous framework significantly increases the electrochemically active surface area offering abundant catalytically active sites and facilitates improved transport of electrolytes. Simultaneously, the heterojunction ensures continuous conductive pathways, thereby minimizing charge-transfer resistance and enhancing overall electron mobility. The combined structural and electronic advantages translate into markedly improved sensitivity, catalytic activity, and operational stability for enzymatic Cr(VI) detection with a limit of detection (LOD) of 39 nM. Overall, the results underscore the significant role of heterojunction engineering in enhancing the performance of metal hydroxide–oxide materials for advanced environmental sensing applications.

1. Introduction

Hexavalent chromium (Cr(VI)) is a highly toxic and carcinogenic pollutant prevalent in industrial effluents, posing significant environmental and health risks. Its reduction to the less toxic trivalent chromium (Cr(III)) and accurate sensing are crucial for environmental remediation and monitoring. The reduction of Cr(VI) to the less harmful Cr(III) is a critical process in detoxifying contaminated water. Chronic exposure to Cr(VI) causes bronchitis and liver, kidney, and nerve tissue damage, and it has been shown to have carcinogenic, mutagenic, and genotoxic effects.[1,2] While the U.S. Environmental Protection Agency (EPA) says that 0.1 mg L^{-1} is the permissible quantity, the World Health Organization (WHO) recommends a tolerable value of 0.050 mg L^{-1} for Cr in drinking water.[3–5] Thus, rapid and effective Cr(VI) detection technology is essential for ensuring the safety of drinking water sources and food products. When it comes to sensing, common detection techniques include X-ray fluorescence, voltammetry, spectrofluorometry, spectrophotometry (colorimetric), inductively coupled plasma atomic emission spectrometry or mass spectrometry, and graphite furnace atomic absorption spectrometry.[6] Despite their extremely high sensitivity, optical atomic spectrometry and mass spectrometry are incompatible with on-site detection and necessitate highly skilled individuals and expensive, complicated equipment to perform. Analyte detection *via* colorimetric techniques is one of the most popular approaches due to its ease of use, particularly when it involves a color shift that is visible to the unaided eye. Nanozymes are a class of nanomaterials that, because of their inherent characteristics, such as size, structure, surface charge, *etc.*, can effectively mimic normal enzymes by catalyzing H_2O_2-mediated reactions.[7,8] For instance, Cr(VI) was detected and quantified utilizing gold amalgam nanocomposites with oxidase capabilities and 3,3′,5,5′-tetramethylbenzidine (TMB) as a substrate.[5] Using polyethylenimine-stabilized Ag nanoclusters, oxidation of TMB by Cr(VI) was employed in a different investigation to detect the same with a broader linearity range of 0.25–5.2 mg L^{-1} and

[a]Department of Chemistry, Jagannath Barooah University, Jorhat, Assam, 785001, India. E-mail: gitashree.darabdhara@gmail.com

[b]Department of Chemistry, D. C. B. Girls College, Jorhat, Assam, 785001, India. E-mail: manashjbom@gmail.com

[c]Department of Chemistry, D. D. R. College, Chabua, Dibrugarh, Assam, 786184, India. E-mail: eramonisaikia@gmail.com; birajdaschm@gmail.com

[d]Department of Chemistry, Dimoria College (Autonomous), Khetri, Kamrup(M), Guwahati, Assam, 782403, India. E-mail: shivaneebgohain@gmail.com

[e]Department of Chemistry, Arya Vidyapeeth College (Autonomous), Guwahati, Assam, 781016, India. E-mail: rajarshibayan@gmail.com

[f]Department of Chemistry, Suren Das College (Autonomous), Kamrup, Hajo, Assam, 781102, India. E-mail: rahulkemprai827@gmail.com; mcotton233@gmail.com

[g]Department of Chemistry, D. H. S. K. College (Autonomous), Dibrugarh, Assam, 786001, India. E-mail: dipankoj2010@rediffmail.com

[h]Department of Mechanical Engineering, Ulsan National Institute of Science and Technology, UNIST-gil 50, Ulju-gun, Ulsan 44919, Republic of Korea. E-mail: ypark@unist.ac.kr

a LOD and LOQ of 0.0572 and 0.1924 mg L^{-1}, respectively.[9] Similarly, in the presence of TMB and H_2O_2, polyethylene glycol-functionalized poly(*N*-phenyl glycine) (PNPG-PEG) nanoparticles were employed to improve the signal for the detection of Cr(VI).[10] Good linearity (0.01–0.1 μM) and LOD (0.012 μM) were attained using the approach. Because of its potent anti-interference properties, non-toxicity, and excellent stability, TMB has been used as a chromogenic chemical in a number of other investigations.[11,12]

The detection of Cr(VI) has significantly advanced with recent developments in nanozyme-based sensing platforms that include use of defect-engineered single-atom catalysts, MOF-based oxidoreductase mimics, and fluorescent carbon nanodots.[13–16] Despite their high sensitivity, many systems suffer from poor structural stability in acidic environments, high substrate affinity, aggregation-induced deactivation, and restricted electron-transfer efficiency.[17] Furthermore, there is still a lack of research on rationally engineered nanoporous heterojunctions that optimize accessibility to catalytic sites and interfacial redox coupling. Therefore, by improving charge transfer, enhancing active site density, and boosting catalytic kinetics for effective Cr(VI) detection, the development of a structurally integrated $Ni(OH)_2/Co_3O_4$ nanoporous heterojunction offers a promising strategy to overcome these limitations.

Bimetallic metal oxides play a crucial role in the sensing and reduction of Cr(VI) due to their enhanced catalytic, electrochemical, and adsorption properties.[18] The incorporation of two different metals into the metal oxide framework often results in synergistic effects that improve performance in environmental applications, particularly in the detection and detoxification of Cr(VI).[19]

The presence of two metals in a metal oxide matrix can create more active sites and enhance electron transfer processes, which are essential for the reduction of Cr(VI).[20] Furthermore, the combination of two metals increases the adsorption capacity for Cr(VI), attributed to the varied oxidation states and coordination environments that bimetallic oxides offer.[21] This enhancement in adsorption is crucial for capturing Cr(VI) ions from contaminated water. Nanoporous heterojunctions based on bimetallic oxides have emerged as promising candidates for Cr(VI) sensing and reduction due to their unique structural and electronic properties.[22] The heterojunction formation facilitates efficient electron transfer, essential for the reduction process. Moreover, the stability and durability of bimetallic oxides under harsh conditions are crucial for practical applications in water treatment and environmental remediation.[22]

In addition to conventional catalytic and nanozyme-based sensing techniques, semiconductor photocatalysis has become a successful method for monitoring pollutants and environmental remediation. Cr(VI) can be degraded more easily with the help of photocatalytic materials, which produce reactive oxygen species owing to photoinduced charge separation.[20,22] Recent developments in plasmonic and hot electron photocatalysis have additionally expanded the potential of catalytic nanomaterials *via* enabling effective utilization of light energy through localized surface plasmon resonance (SPR) and energetic charge carriers.[23] Hot-electron-mediated processes can greatly improve interfacial redox reactions by enhancing charge injection and suppressing recombination losses.[23,24] These new concepts emphasize the effectiveness of electron-transfer routes and interfacial charge transport in catalytic nanostructures.[25,26]

While our present work is focused on colorimetric sensing using nanozymes rather than photocatalysis, the design of nanoporous $Ni(OH)_2/Co_3O_4$ heterojunctions is fundamentally similar to photocatalytic systems in terms of heterointerface-driven charge separation and improved catalytic activity. By optimizing the interface between $Ni(OH)_2$ and Co_3O_4, we enable efficient electron transfer pathways that are vital for both nanozymatic oxidation of TMB and the potential photocatalytic detoxification of industrial effluents.

Highlighting the critical role of nanoporous materials, this article explores the synthesis, characterization, and catalytic capabilities of the nanoporous $Ni(OH)_2/Co_3O_4$ heterojunction in Cr(VI) sensing. Employing a multidisciplinary approach spanning chemistry, materials science, and environmental engineering, this research aims to advance the development of efficient, sustainable strategies for mitigating hazardous pollutants and safeguarding environmental integrity. The novelty of the present work lies in the rational design of a nanoporous $Ni(OH)_2/Co_3O_4$ heterojunction that integrates interfacial redox coupling with a high-surface-area nanoarchitecture to enhance peroxidase-like catalytic performance. In contrast to previously documented mono-metallic or randomly built bimetallic nanozymes, the developed interface enables faster electron transfer between Ni^{2+} and Co^{2+}/Co^{3+} centres that contributes to improving the formation of reactive oxygen species, which helps in the detection of Cr(VI). Heterojunction-mediated charge transport in combination with nanoporous morphology offers an effective catalytic enhancement method for stable and sensitive Cr(VI) colorimetric detection.

2. Materials and methods

2.1. Materials

Cobalt chloride ($CoCl_2$) and nickel chloride ($NiCl_2 \cdot 6H_2O$) were purchased from E-Merck, India. Sodium hydroxide (NaOH) was brought from E-Merck. 4-Nitrophenol and sodium borohydride ($NaBH_4$) were received from Sigma-Aldrich, Germany. $K_2Cr_2O_7$ was purchased from E-Merck, India. 3,3′,5,5′-Tetramethylbenzidine (TMB) was purchased from Sigma-Aldrich, USA. All the chemicals were used as received and without any further purification.

2.2. Instrumental techniques

The Fourier-transform Infrared Spectroscopy (FT-IR) spectrum was recorded in the mid-IR range of 450–4000 cm^{-1} using a Frontier-MIR-FIR from PerkinElmer. The FT-IR spectra of solid samples were recorded in DRIFT mode by grinding the samples with KBr. Powder X-ray diffraction (PXRD) measurements were recorded using a BRUKER AXS D8 FOCUS

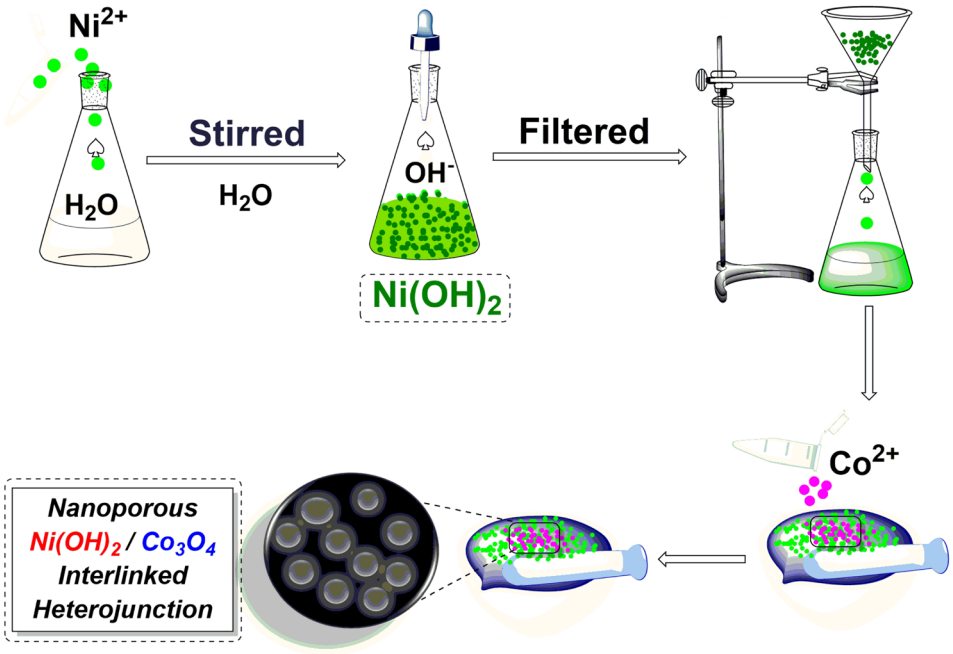

Scheme 1 A schematic illustration for the synthesis of $Ni(OH)_2/Co_3O_4$.

instrument in low angle mode at 2θ values ranging between 10–80°. Raman analyses were done on a Horiba LabRAM HR spectrophotometer equipped with a He–Ne laser with an excitation wavelength of 514.5 nm. The electronic absorption spectrum was recorded using a SHIMADZU UV-2600i spectrophotometer. The XPS analysis was carried out on an ESCALAB Xi+ (Thermo Fisher Scientific Pvt. Ltd, UK). A UV/visible spectrophotometer (SPECORD-200, Analytik Jena, Germany) was used to measure the produced nanocomposite's peroxidase activity toward Cr(VI) detection.

2.3. Synthesis of the bimetallic nanocatalyst, $Ni(OH)_2/Co_3O_4$

To synthesize the nanocatalyst, 14.4 mg of nickel chloride ($NiCl_2 \cdot 2H_2O$) is dissolved in 100 mL of water. A concentrated solution of sodium hydroxide (NaOH) is then added until complete precipitation of nickel hydroxide, $Ni(OH)_2$, occurs. The resulting precipitate is washed several times with hot water and subsequently dried in an oven. Next, the dried $Ni(OH)_2$ precipitate is meticulously mixed with 7.5 mg of cobalt chloride ($CoCl_2$) in a mortar and pestle for 8 h. The resulting mixture is washed repeatedly with hot water to eliminate any impurities present, followed by drying in an oven at 100 °C to obtain the final bimetallic $Ni(OH)_2/Co_3O_4$ nanocatalyst (Scheme 1).

2.4. Investigation of $Ni(OH)_2/Co_3O_4$ peroxidase-like properties

Chromogenic TMB molecules are effectively oxidized by $Ni(OH)_2/Co_3O_4$ to produce an oxidized blue-colored TMB product (Ox-TMB). The standard procedure involved adding 100 μL of $Ni(OH)_2/Co_3O_4$ (50 mg L^{-1}) to a 0.5 mM TMB solution in an acetate buffer of pH 4. After adjusting the reaction mixture's volume to 3 mL and adding 50 μL of H_2O_2 (30%) solution, the mixture was incubated for 20 min at 25 °C in a water bath shaker. The Ox-TMB product was monitored using a UV-visible spectrophotometer at a λ_{max} value of 652 nm. Different parameters such as the concentration of $Ni(OH)_2/Co_3O_4$, the pH of the reaction mixture and temperature were investigated. Next, the temperature and initial pH of the reaction mixture were changed in order to examine the TMB oxidation processes.

By adjusting TMB and H_2O_2 within a specific concentration range, typical Michaelis–Menten curves for the $Ni(OH)_2/Co_3O_4$ nanocomposite were produced. The Michaelis–Menten constant (K_m) and the Lineweaver–Burk double reciprocal plot were used to calculate the enzyme's affinity for the substrate. The Lineweaver–Burk plot uses the following equation:

$$\frac{1}{v} = \left(\frac{K_m}{V_m}\right)\left(\frac{1}{[S]}\right) + \left(\frac{1}{V_m}\right) \quad (1)$$

where v = initial velocity; V_m = maximal reaction velocity; and [S] = substrate concentration.

2.5. Colorimetric detection of Cr(VI) in aqueous solution

The detection of Cr(VI) in aqueous media was used to investigate the nanozymatic detection activity of the $Ni(OH)_2/Co_3O_4$ nanocomposite. Separate additions of Cr(VI) (50–500 nM concentrations) were made to the reaction mixture, which contained 50 μL H_2O_2 (30%) in a buffer solution of pH 3, 0.5 mM TMB, and 100 μL $Ni(OH)_2/Co_3O_4$ nanocomposite. Following this, Cr(VI) detection was performed using changes in UV-vis absorbance intensities at 652 nm for the Ox-TMB product. In order to investigate the selectivity of the $Ni(OH)_2/Co_3O_4$ nanocomposite, 200 nM of various interfering ions, namely Pb(II), Na(I), Cu(II), Hg(II), As(III), K(I), Cd(II), and Co(II), were added to the reaction mixture in a manner as described above.

3. Results and discussion

3.1. Characterization of the $Ni(OH)_2/Co_3O_4$ heterojunction

Transmission electron microscopy (TEM) was employed to assess the crystallinity and confirm the morphology of the synthesized $Ni(OH)_2/Co_3O_4$ heterojunctions. The TEM images presented in Fig. 1 illustrates the nanoporous morphology of the $Ni(OH)_2/Co_3O_4$ nanocomposite, with $Ni(OH)_2$ interlinked with Co_3O_4 nanocrystals. Fig. 1a–c demonstrate a homogenous formation of nanopores, with dimensions approximately ranging from 6 to 10 nm, clearly showcasing the heterojunction structures. High-resolution TEM (HRTEM) analysis (Fig. 1d) reveals an interplanar spacing of about 0.24 nm, which corresponds to the spacing between the (311) crystal planes of the $Ni(OH)_2/Co_3O_4$ nanocomposite.[27] This interplanar spacing is indicative of the crystalline nature and confirms the successful synthesis of the heterojunction material, which is also supported by the SAED pattern of the synthesised material (inset of Fig. 1d). We have calculated the average crystallite size of the nanoporous $Ni(OH)_2$ interlinked Co_3O_4 heterojunction using the Scherrer equation based on the XRD data provided.[28,29]

This calculated value is in excellent agreement with the TEM analysis, which shows a homogenous formation of nanocrystals and nanopores with dimensions ranging from 6 to 10 nm. The calculated size supports the HRTEM observation of an interplanar spacing of 0.24 nm for the (311) crystal planes, confirming high crystallinity within these small domains.

These findings are significant as they underscore the nanoporous architecture of the synthesized material, which is crucial for enhancing the catalytic activities.

In the XRD spectra, the peaks at 31, 39.3, 43.8 and 56.1 correspond to Co_3O_4 and peaks correspond to $Ni(OH)_2$ were observed at 2θ values of 37.5, 46, and 61, as shown in Fig. 2a.[27,30]

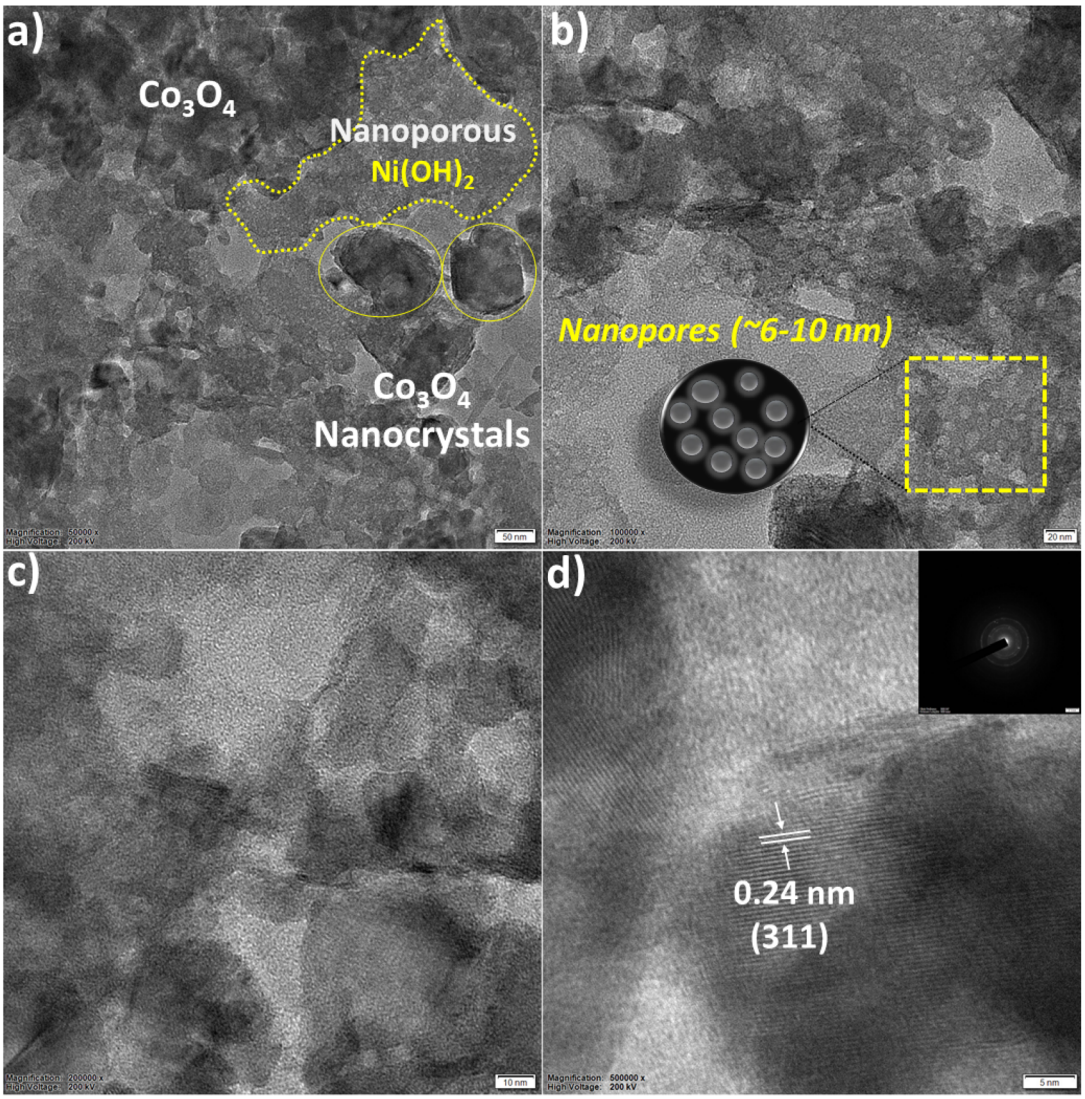

Fig. 1 TEM images of the synthesized $Ni(OH)_2/Co_3O_4$ heterojunctions. (a–c) Formation of nanopores in the dimension range of ~6–10 nm, illustrating the interconnected structure. (d) HRTEM image showing an interplanar spacing of about 0.24 nm (inset of (d) shows the selected area electron diffraction, SAED pattern).

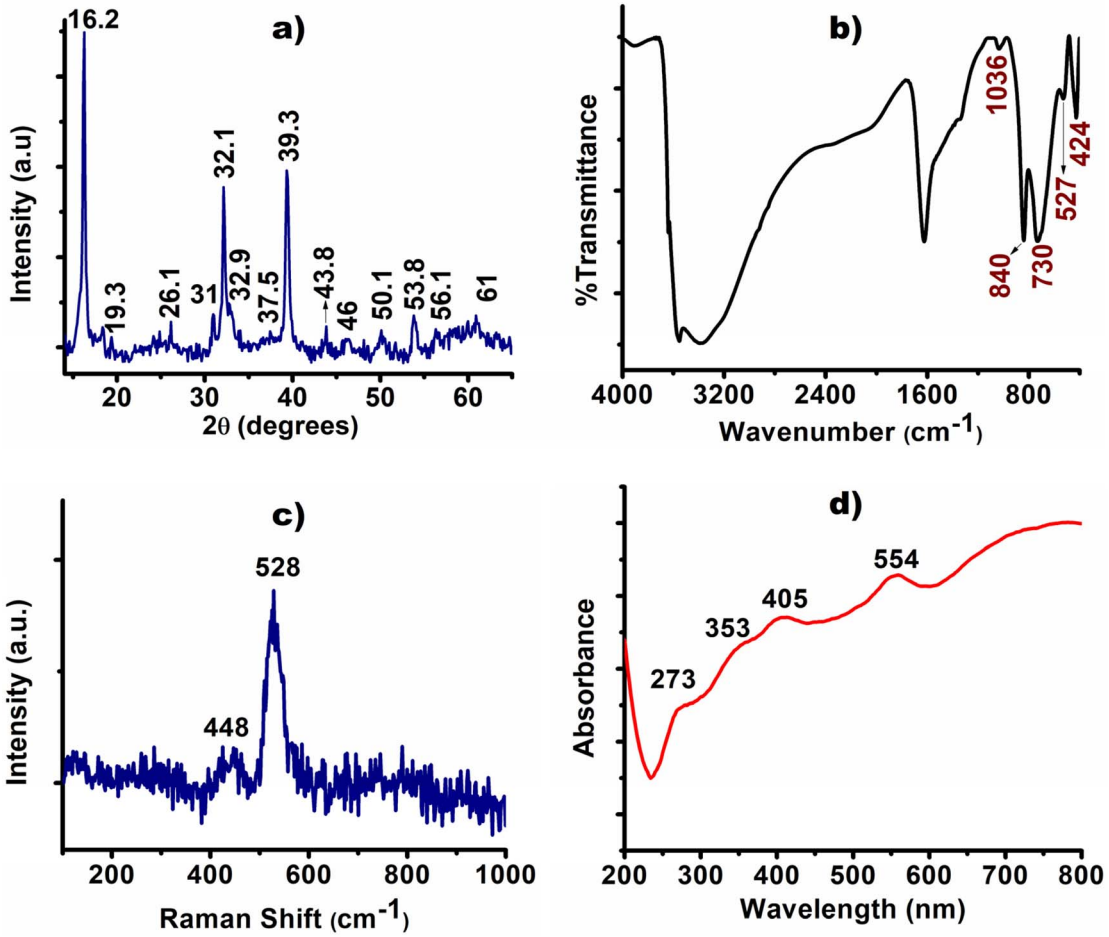

Fig. 2 (a) XRD, (b) FT-IR, (c) Raman and (d) UV-DRS analysis of the $Ni(OH)_2/Co_3O_4$ nanocomposite.

In the FT-IR spectra, the peak at 418 cm^{-1} is assigned to the Ni–O stretching band of $Ni(OH)_2$. Additionally, the spinel structure of the material exhibits characteristic vibrational bands at 530 cm^{-1} and 730 cm^{-1}, which correspond to the Co^{2+}–O vibrations in the tetrahedral sites and the Co^{3+}–O vibrations in the octahedral sites of the Co_3O_4 unit, respectively (Fig. 2b).[27,31] The Raman spectra of the synthesized $Ni(OH)_2/Co_3O_4$ clearly display peaks at 448 and 528 cm^{-1}, which evidently demonstrate the presence of both Ni–O and Co_3O_4 units in the $Ni(OH)_2/Co_3O_4$ composite (Fig. 2c).[27] From the UV-DRS spectra, the absorption peak at 273 nm corresponds to $O^{2-} \rightarrow Co^{2+}$ and that at 554 nm corresponds to the $O^{2-} \rightarrow Co^{3+}$ charge transfer transition of the Co_3O_4 unit.[32,33] The peaks observed at 353 and 405 nm could be attributed to the Ni–O transition in $Ni(OH)_2$ NPs, Fig. 2d.[34]

The crystalline nature and phase purity of the nanoporous $Ni(OH)_2/Co_3O_4$ heterojunction were evaluated using PXRD and TEM-SAED analysis. The average crystallite size was calculated to be approximately ~9.5 nm using the Scherrer equation and the detailed calculation is provided in the SI.[35] This is in excellent agreement with the TEM observations, which reveal interlinked nanocrystals and nanopores within the 6–10 nm range. The calculated size supports the HRTEM observation of an interplanar spacing of 0.24 nm for the (311) crystal planes, confirming high crystallinity within these small domains.[36,37]

Based on X-ray Photoelectron Spectroscopy (XPS) spectra, the presence of Co and Ni was confirmed based on distinctive peaks and binding energies. Binding energy values found at 856.3 eV for $2p_{3/2}$ and 873.9 eV for $2p_{1/2}$ correspond to Ni^{2+} in $Ni(OH)_2$.[38] The satellite peaks at 862.1 eV and 880.6 eV further support the presence of NiO (Fig. 3a).[39] Binding energy values observed at 781.6 eV and 798.1 eV for $2p_{3/2}$ and $2p_{1/2}$, respectively, indicate the presence of Co^{2+}. After deconvolution, the peak at 796.5 eV confirms the presence of Co^{3+} in the synthesized material.[40] The satellite peaks observed at 786.1 eV and 803.2 eV were characteristic of the spinal structure of the synthesized material, also confirmed by FTIR analysis (Fig. 3b).[40] These findings confirm the formation of Co_3O_4 and $Ni(OH)_2$ in the analysed sample, providing valuable insight into its chemical composition and structure. Zhao *et al.* also observed similar binding energy values in the spinal structure of the synthesized Co_3O_4 nanostructures.[41] In the oxygen (O) spectra of the synthesized material, two peaks appeared after deconvolution at 530.7 eV and 531.5 eV, indicative of different O binding sites (Fig. 3c).[42] The peak found at 530.7 eV is attributed to metal oxide formation and that at 531.5 eV is attributed to oxygen vacancies.[42]

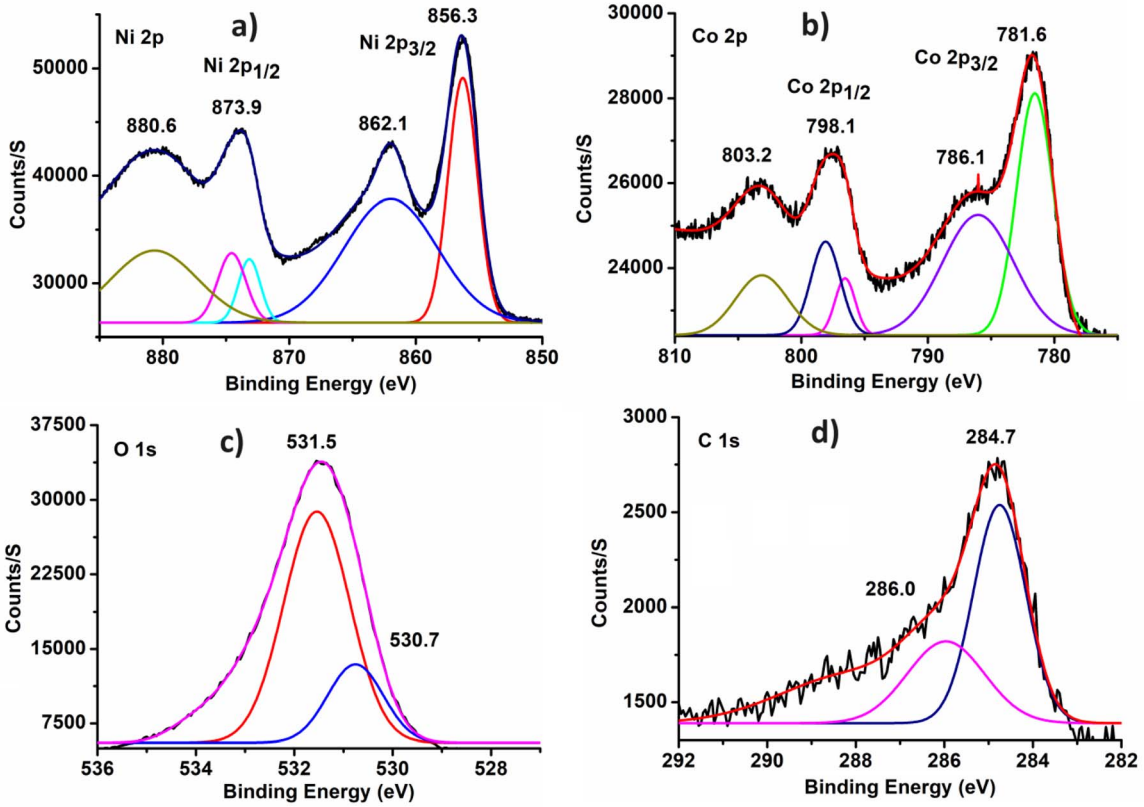

Fig. 3 XPS spectra of (a) Ni 2p, (b) Co 2p, (c) O 1s, and (d) C 1s of the synthesized $Ni(OH)_2/Co_3O_4$ nanocomposite.

Carbon (C) spectra of the material revealed two peaks at binding energy values of 284.7 eV for C–C bonds and 286.0 eV for the presence of O–C═O groups, respectively, Fig. 3d.[40]

3.2. $Ni(OH)_2/Co_3O_4$ nanocomposite's intrinsic peroxidase-like activity and reaction condition optimization

The oxidation reaction of TMB in the presence of H_2O_2 was used to investigate the peroxidase-like activity of the $Ni(OH)_2/Co_3O_4$ nanocomposite. The resulting blue colored oxidized product of TMB showed absorbance maxima at 652 nm due to the formation of 3,3′,5,5′-tetramethylbenzidine diimine (TMBDI).[43]

To illustrate the $Ni(OH)_2/Co_3O_4$ nanocomposite's peroxidase-like catalytic activity, the oxidation of TMB was investigated under various conditions. $Ni(OH)_2/Co_3O_4$ nanocomposite-catalyzed TMB oxidation was carried out as a control without H_2O_2. Since there was no color change, it can be concluded that TMB oxidation requires both H_2O_2 and the $Ni(OH)_2/Co_3O_4$ nanocomposite. The peroxidase-like catalytic activity towards TMB oxidation was found to be significantly higher when the reaction was conducted in the presence of the catalyst as well as H_2O_2. The changes observed due to the oxidation of TMB are depicted in Fig. 4.

It was possible to determine the ideal analytical conditions by examining how the pH, temperature, and catalyst quantity affected the peroxidase-like activity of the $Ni(OH)_2/Co_3O_4$ catalyst. Fig. 5A shows how pH affects the activity of the $Ni(OH)_2/Co_3O_4$ catalyst. The catalytic activity of $Ni(OH)_2/Co_3O_4$ quickly declines beyond pH 3, which is also the pH at which maximum absorbance is seen. At a concentration of 100 mg L^{-1} of $Ni(OH)_2/Co_3O_4$ nanocomposite, the maximum catalytic activity was observed at 25 °C (Fig. 5B, C). Thus, the following

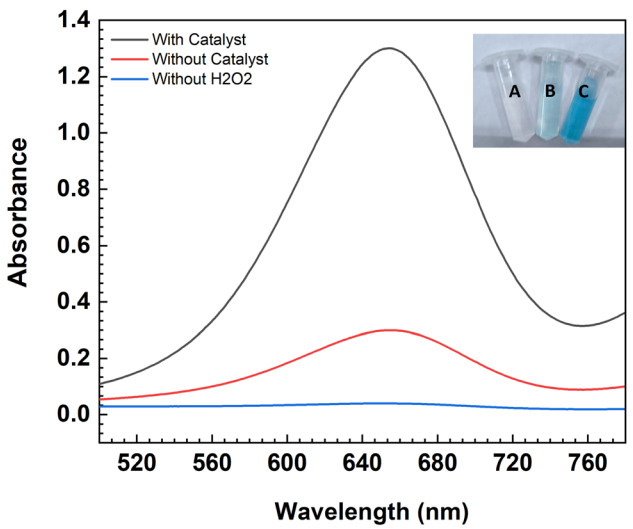

Fig. 4 UV-visible spectrum of 0.5 mM TMB without H_2O_2, without the $Ni(OH)_2/Co_3O_4$ nanocomposite and in the presence of both H_2O_2 and the $Ni(OH)_2/Co_3O_4$ nanocomposite. The inset shows the corresponding photographs (A = without H_2O_2; B = without the $Ni(OH)_2/Co_3O_4$ nanocomposite but in the presence of H_2O_2; C = presence of both the $Ni(OH)_2/Co_3O_4$ nanocomposite and H_2O_2).

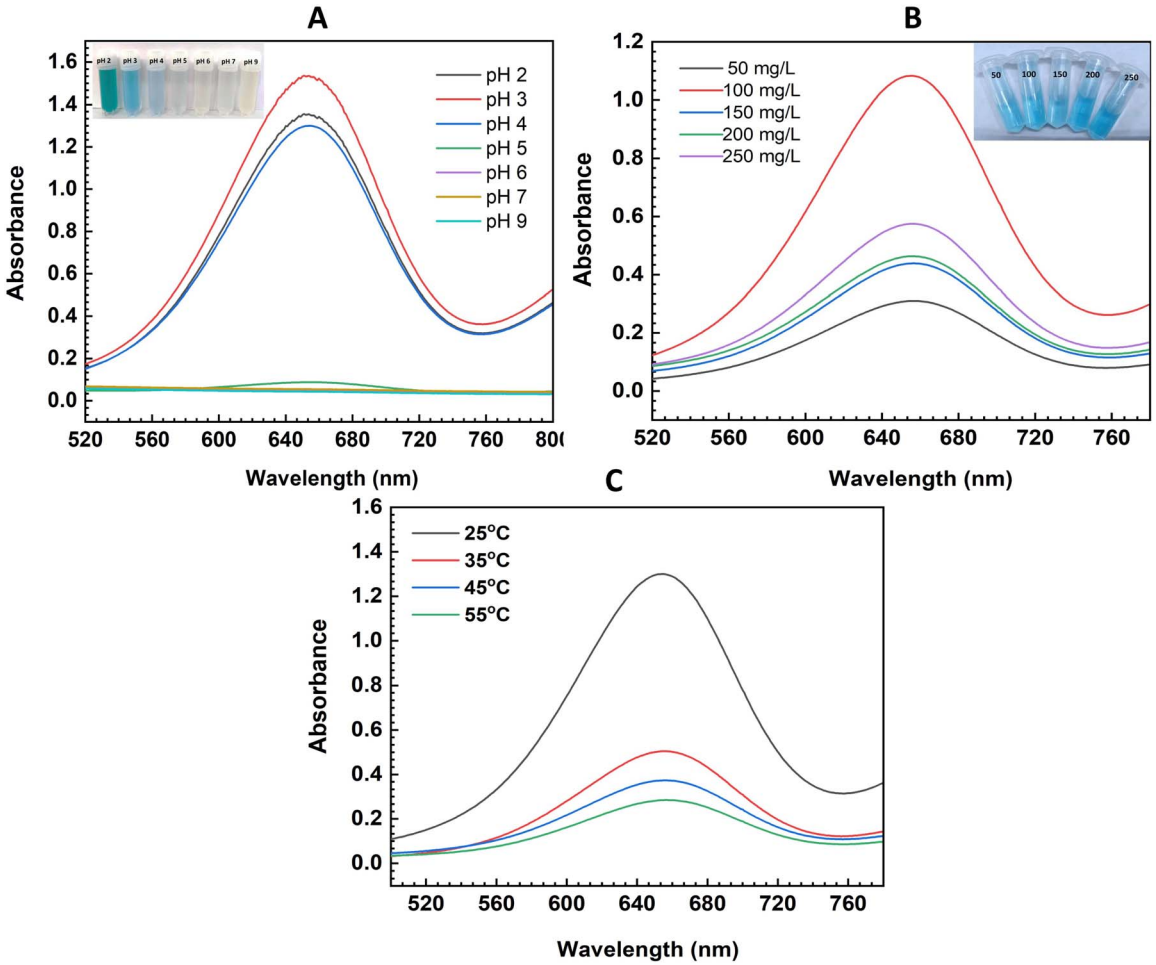

Fig. 5 UV-visible absorption spectra for oxidation of TMB using the $Ni(OH)_2/Co_3O_4$ nanocomposite at different (A) pH values, (B) catalyst concentrations and (C) temperatures.

circumstances result in the highest catalytic activity: 100 mgL^{-1} of $Ni(OH)_2/Co_3O_4$ nanocomposite at pH 3 and 25 °C.

3.3. Kinetic evaluation of the $Ni(OH)_2/Co_3O_4$ nanocomposite as a peroxidase mimic and determination of the Michaelis constant

Utilizing steady state kinetics and the initial rate approach, the intrinsic peroxidase-like catalytic activity of the $Ni(OH)_2/Co_3O_4$ nanocomposite was examined utilizing TMB and H_2O_2 as substrates. While maintaining a constant concentration of the other reagents, kinetic analysis was carried out by varying the concentration of the substrates (TMB and H_2O_2). Beer–Lambert law was used to convert the absorbance readings to their respective concentrations:

$$A = \varepsilon_{TMBDI} \times c \times L \quad (2)$$

where ε_{TMBDI} = 39 000 M^{-1} cm^{-1} at 652 nm for TMBDI, c = concentration of the sample and L refers to the path length.[44]

Typical Michaelis Menten curves for TMB and H_2O_2 (shown in Fig. 6A and B, respectively), as substrates in a certain concentration range, were produced by converting the appropriate concentration terms to velocity terms. Lineweaver–Burk double reciprocal plots were then used to determine the catalytic parameters K_m (Michaelis constant) and V_m (maximal velocity) of the enzyme mimics $Ni(OH)_2/Co_3O_4$. The slope of the Lineweaver–Burk double reciprocal plots (as shown in the insets of Fig. 6A and B) yields the value of K_m, while their intercept yields the value of V_m. The K_m value of $Ni(OH)_2/Co_3O_4$ for TMB as a substrate was found to be 0.53 mM whereas that for H_2O_2 was found to be 2.42 mM. The corresponding V_m values for TMB and H_2O_2 as substrates were found to be 4.77×10^{-8} M s^{-1} and 2.80×10^{-8} M s^{-1}, respectively.

The low K_m value (0.53 mM for TMB) for $Ni(OH)_2/Co_3O_4$ suggests that it has a higher substrate affinity for TMB. Additionally, compared to many other enzyme mimics as shown in Table S1, the K_m value reported for $Ni(OH)_2/Co_3O_4$ with H_2O_2 is significantly lower, indicating that a lower H_2O_2 concentration is needed for TMB oxidation.

3.4. Plausible mechanism of the peroxidase-like activity

The pertinent reactive species in the catalytic system were observed in order to examine the catalytic mechanism of the

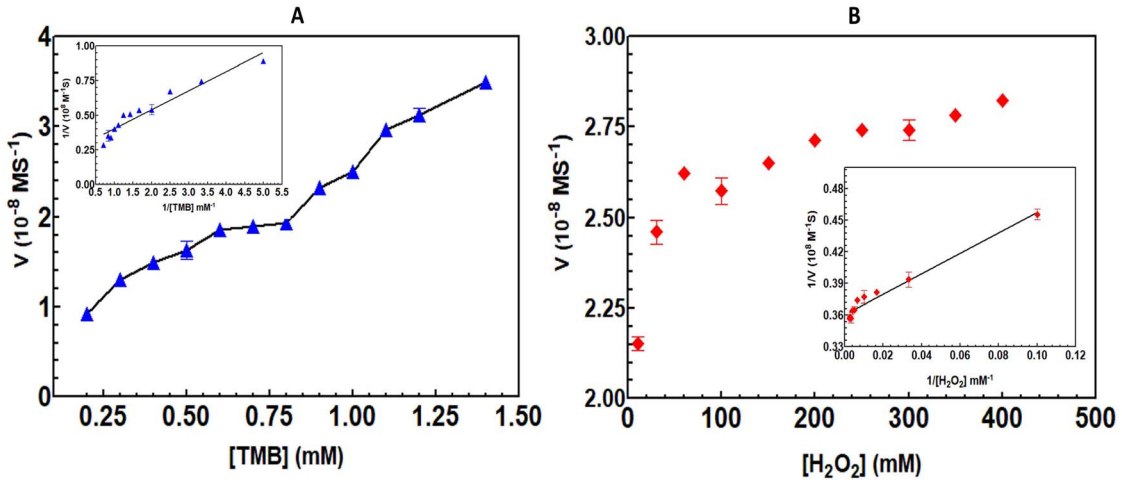

Fig. 6 $Ni(OH)_2/Co_3O_4$ nanocomposites' catalytic mechanism and steady-state kinetic assay. (A) TMB concentration variation at a fixed H_2O_2 concentration (50 mM). (B) H_2O_2 concentration variation at a fixed TMB concentration (0.5 mM). The inset displays the matching Lineweaver–Burk plots of the double reciprocal of the Michaelis Menten equation.

peroxidase-like activity of the $Ni(OH)_2/Co_3O_4$ nanocomposites. The peroxidase-like activities of nanozymes catalyse the generation of hydroxyl radicals ($^{\bullet}OH$) from hydrogen peroxide (H_2O_2), which in turn oxidizes the chromogenic substrate to produce the blue colour. $Ni(OH)_2/Co_3O_4$ nanocomposites exhibit strong peroxidase-mimicking activity as a result of their Fenton-like behavior in the presence of H_2O_2. TMB molecules are adsorbed onto the surface of the $Ni(OH)_2/Co_3O_4$ nanocomposites. The adsorption of TMB molecules onto the surface of the $Ni(OH)_2/Co_3O_4$ nanocomposite surface occurs through π–π interactions between their functional groups. $Ni(OH)_2/Co_3O_4$ facilitates Fenton reactions that generate $^{\bullet}OH$ radicals from H_2O_2. The reactions involved in the Fenton process are shown in the equations below (eqn (3)–(5)).[45,46]

Co_3O_4 has mixed valence states (Co^{2+} and Co^{3+}) that accelerate Fenton-like reactions to break down H_2O_2.

$$Co^{2+} + H_2O_2 \rightarrow Co^{3+} + OH^- + {}^{\bullet}OH \quad (3)$$

$$Co^{3+} + H_2O_2 \rightarrow Co^{2+} + H_2O + HOO^{\bullet} \quad (4)$$

The $^{\bullet}OH$ radical, being a powerful oxidizing species, converts TMB into blue-colored Ox-TMB, which exists in equilibrium with the cation free radical $TMB^{+\bullet}$.

$$TMB + {}^{\bullet}OH \rightarrow \text{Ox-TMB (blue colour)} \quad (5)$$

Although we could not quantify the decomposition of H_2O_2 (as it was used in a significantly lower amount, 50 μL), its role in generation of $^{\bullet}OH$ can be evaluated using a fluorescent method using terephthalic acid (TA) as a probe molecule. TA reacts selectively with $^{\bullet}OH$ to form 2-hydroxyterephthalic acid (TAOH) that shows a characteristic fluorescence emission at 410 nm. The excitation and emission wavelengths are at 315 nm and 410 nm, respectively. The fluorescence signal of TAOH confirms the formation of $^{\bullet}OH$ in the reaction system. In a typical experiment, an optimized amount of the catalysts (100 mg L^{-1})

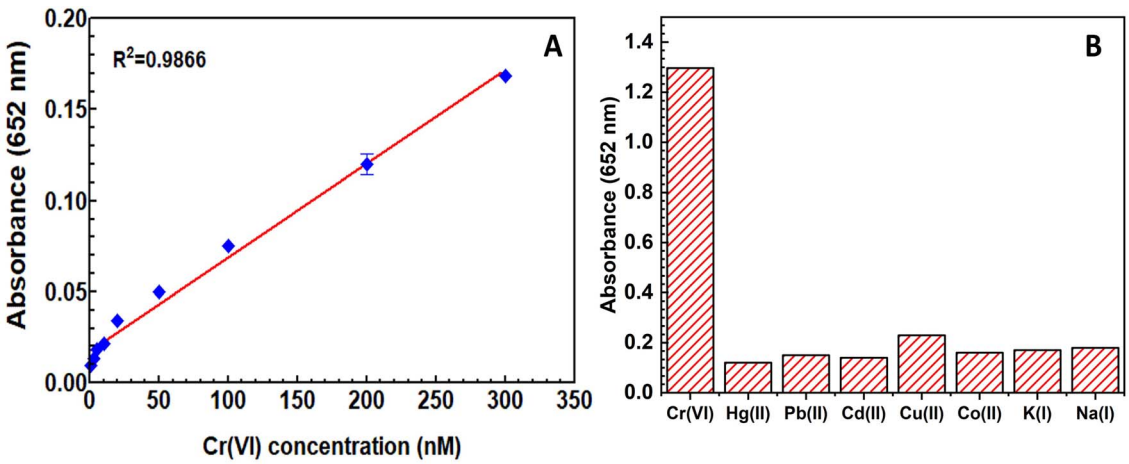

Fig. 7 (A) Standard Cr(VI) concentration response curve under optimum conditions using the $Ni(OH)_2/Co_3O_4$ nanocomposite and (B) selectivity study of Ox-TMB absorbance following the sensing process in the presence of various inorganic ions.

Table 1 Evaluation of the activity of $Ni(OH)_2/Co_3O_4$ towards colorimetric Cr(VI) detection activity in comparison to previously published materials

Sl. no.	Material	Linear range	Limit of detection	Reference
1	N- and S-doped carbon dots	1–40 μM	0.52 μM	50
2	Ag–Ag nanocluster	0.6–10 μM	0.3 μM	51
3	Graphene QDs	1–500 μM	190 nM	52
4	CuS/Fe_3O_4	0–1500 μM	60 nM	53
5	Fe_3O_4@MQDs	0–60 μM	0.26 nM	54
6	Cu-PyC MOF	0.5–50 μM	0.051 μM	55
7	PNPG-PEG	0.05–12.5 μM	520 nM	10
8	$CoFe_2O_4/H_2PPOP$	0.6–100 μM	0.026 μM	56
8	$Ni(OH)_2/Co_3O_4$	10–300 nM	39 nM	This work

was dispersed in an aqueous TA/NaOH solution (1 : 2 molar ratio) containing 50 μL H_2O_2. The fluorescence spectra were recorded at 5 min and 20 min (as shown in Fig. S1, in SI). The enhanced PL intensity at 20 min indicates a more efficient generation of $^{\bullet}OH$ compared to that at 5 min. Since fluorescence intensity at 410 nm is directly proportional to $^{\bullet}OH$ production, the stronger emission confirms higher $^{\bullet}OH$ generation, leading to faster and more efficient TMB oxidation.

3.5. Detection of Cr(VI) using $Ni(OH)_2/Co_3O_4$ nanocomposites and selectivity study

The nanozymatic detection technique has garnered significant attention in the last years because of its simplicity, convenience of use without a sophisticated instrument, and visibility to the unaided eye.[47] Accordingly, the $Ni(OH)_2/Co_3O_4$ nanocomposite was also effectively used for the colorimetric detection of Cr(VI) due to its superior peroxidase-like activity, as was previously mentioned.

Typically, in an acetate buffer of pH 3, $Ni(OH)_2/Co_3O_4$ nanocomposites, H_2O_2 (30%) and TMB under their optimum conditions were allowed to mix with varying quantities of freshly prepared Cr(VI) solutions (1–300 nM) and allowed to react with the reaction mixture at 25 °C. At a wavelength of 652 nm, the Ox-TMB product's UV-Vis absorbance variations were observed for these various Cr(VI) concentrations. As the concentration of Cr(VI) rose, the absorbance intensity for the Ox-TMB product increased progressively. In acidic media, Cr(VI) can break down H_2O_2 into O_2 and H_2O. Fenton reactions allow both O_2 and H_2O to combine with electrons on the surface of $Ni(OH)_2/Co_3O_4$ to form $^{\bullet}OH$. As a result, when Cr(VI) is present in the reaction mixture, TMB oxidation rises.[48] The absorbance at 652 nm *vs.* concentration of Cr(VI) was plotted to create a calibration curve based on the variations in absorbance intensity, as shown in Fig. 7A. In the linear range of 10–300 nM, the LOD for Cr(VI) detection was found to be 39 nM. Comparing $Ni(OH)_2/Co_3O_4$ activity to that of the majority of other previously published nanomaterials (Table 1) for colorimetric detection of Cr(VI), the LOD is noticeably lower.

In the presence of 200 nM of various interfering ions, including Hg(II), Pb(II), Cd(II), Cu(II), Co(II), K(I), and Na(I), the selectivity of $Ni(OH)_2/Co_3O_4$ was also examined in the colorimetric detection of Cr(VI), as shown in Fig. 7B. The presence of Cr(VI) significantly boosts the TMB oxidation efficiency, most likely as a result of the ions' strong catalytic sites and adsorption at the $Ni(OH)_2/Co_3O_4$ surface. Although not as strongly as with Cr(VI), other metal ions also interact with the surface of $Ni(OH)_2/Co_3O_4$.[49] When Cr(VI) was present, there was a noticeable rise in the Ox-TMB absorption intensity.

3.6. Detection of Cr(VI) ions in environmental samples

The synthesized materials' practical sensor application for the detection of the Cr(VI) ion in various environmental samples was

Table 2 Measurement of Cr(VI) in real-world samples

Sample	Cr(VI) added (nM)	Cr(VI) detected (nM)	Recovery (%)
Tap water	10	9.94	99.40
	50	49.72	99.44
	100	99.50	99.50
Pond water	10	10.1	101.00
	50	49.20	98.40
	100	98.47	98.47
Well water	10	9.61	96.10
	50	48.80	97.60
	100	97.52	97.52

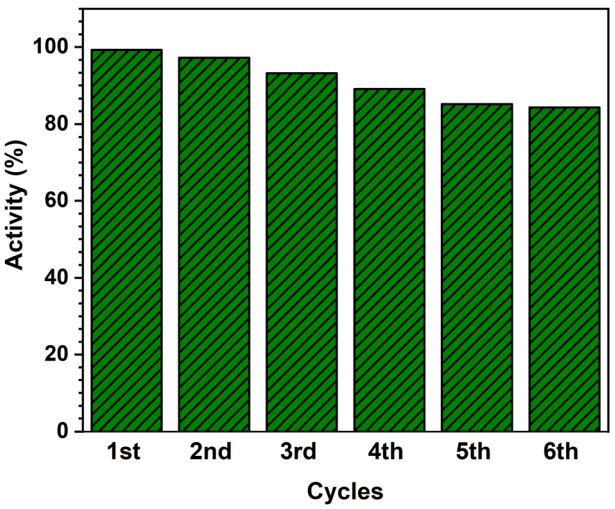

Fig. 8 Reusability study of the $Ni(OH)_2/Co_3O_4$ nanocomposite for the TMB oxidation reaction.

examined. Table 2 shows the relative standard deviation and recovery % for the various environmental samples. In several environmental samples, the suggested approach demonstrated a good recovery % for Cr(VI). The findings imply that the suggested sensor can be utilized to detect Cr(VI) in actual samples with good recovery values.

3.7. Reusability study of the $Ni(OH)_2/Co_3O_4$ nanocomposite

By performing the reaction six times, the reusability of the $Ni(OH)_2/Co_3O_4$ nanocomposite as an enzyme mimic for TMB oxidation was examined. After six catalytic cycles, the relative activity was 84.32% of the initial activity, as illustrated in Fig. 8. According to the results, the $Ni(OH)_2/Co_3O_4$ nanocomposite is a nano-enzyme with superior stability and catalytic activity.

We have performed a PXRD analysis on the catalyst recovered after five consecutive cycles. The post-catalysis PXRD pattern (now included as Fig. S2 in the SI) shows no significant shift in peak positions or emergence of new phases. This indicates that the heterojunction maintains its structural integrity and phase stability during the sensing of chromium(VI), justifying its excellent reusability. Sensors often face surface poisoning or phase transformation. By showing that the Co_3O_4 and $Ni(OH)_2$ peaks remain unchanged after use, we demonstrate that the detection mechanism is likely surface-redox driven rather than a destructive chemical reaction, confirming the robustness of the material as claimed in the Abstract.

4. Conclusion

In conclusion, we have successfully designed and synthesized a nanoporous $Ni(OH)_2/Co_3O_4$ heterojunction and demonstrated its enhanced peroxidase-like activity for sensitive colorimetric detection of Cr(VI). Integrating engineered heterointerfaces into nanoporous structures has effectively enhanced both catalytic and sensing efficiency. The development of a distinct heterojunction was confirmed by structural analysis, whereas kinetic studies established improved substrate affinity and effective H_2O_2 activation due to synergistic Ni^{2+}–Co^{2+}/Co^{3+} redox coupling. The developed heterojunction delivered a limit of detection of 39 nM, a 10–300 nM linear range and high selectivity for Cr(VI) together with satisfactory stability and reliability in real-sample detection.

This study validates that rational design of heterointerfaces is crucial in advancing metal hydroxide–oxide catalysts. Bridging the gap between materials science and device engineering will be essential for developing the next generation of portable environmental diagnostic tools.

Conflicts of interest

There are no conflicts to declare.

Data availability

The data supporting the findings of this study are available from the corresponding author upon request.

Supplementary information (SI): Scherrer equation calculation, comparison of kinetic parameters of synthesized nanocomposites with other reported materials, photoluminescence spectra (PL) of TMB oxidation reaction confirming the generation of $^{\bullet}OH$ radicals, PXRD analysis on the catalyst recovered after five consecutive cycles. See DOI: https://doi.org/10.1039/d5na01116g.

Acknowledgements

BD, MS, and MJB sincerely acknowledge DDR College, Dibrugarh, Suren Das College (Autonomous), Kamrup, and DCB Girls College, Jorhat, Assam, India, for the analytical facilities provided to perform the experimental studies. The authors also thank SAIC-Tezpur University for the instrumentation facilities. GD acknowledges the laboratory facilities of CSIR-NEIST, Jorhat.

References

1 W. Jin and K. Yan, *RSC Adv.*, 2015, **5**(47), 37440–37450, DOI: 10.1039/c5ra03480a.
2 M. Li and S. Zhou, *Chem. Eng. J.*, 2018, **339**, 539–546, DOI: 10.1016/j.cej.2018.02.002.
3 M. Loock, J. Beukes and P. Van Zyl, *Water*, 2014, **40**(4), 709, DOI: 10.4314/wsa.v40i4.16.
4 A. Sheikhmohammadi, S. M. Mohseni, R. Khodadadi, M. Sardar, M. Abtahi and S. Mahdavi, *J. Mol. Liq.*, 2017, **233**, 75–88, DOI: 10.1016/j.molliq.2017.02.101.
5 X. Zhang, W. Liu, X. Li, Z. Zhang, D. Shan, H. Xia, S. Zhang and X. Lu, *Anal. Chem.*, 2018, **90**(24), 14309–14315, DOI: 10.1021/acs.analchem.8b03597.
6 P. K. Boruah, G. Darabdhara, P. Borthakur, B. L. Ouay and M. R. Das, *Chem. Eng. J.*, 2023, **474**, 145797, DOI: 10.1016/j.cej.2023.145797.
7 F. Manea, F. B. Houillon, L. Pasquato and P. Scrimin, *Angew. Chem., Int. Ed.*, 2004, **43**(45), 6165–6169, DOI: 10.1002/anie.200460649.
8 J. Wu, X. Wang, Q. Wang, Z. Lou, S. Li and Y. Zhu, *Chem. Soc. Rev.*, 2018, **48**(4), 1004–1076, DOI: 10.1039/c8cs00457a.
9 J. Li, H. Wei, S. Guo and E. Wang, *Anal. Chim. Acta*, 2008, **630**(2), 181–185, DOI: 10.1016/j.aca.2008.10.004.
10 S. Ghayyem, A. Swaidan, A. Barras, M. Dolci, F. Faridbod and S. Szunerits, *Talanta*, 2021, **226**, 122082, DOI: 10.1016/j.talanta.2021.122082.
11 Y. Qi, J. Ma, F. R. Xiu and X. Gao, *Microchim. Acta*, 2021, **188**(8), 273, DOI: 10.1007/s00604-021-04942-7.
12 Q. Xue, X. Li, Y. Peng, P. Liu, H. Peng and X. Niu, *Microchim. Acta*, 2020, **187**(5), 263, DOI: 10.1007/s00604-020-04232-8.
13 D. C. Onwudiwe, N. Gobile, O. A. Oyewo and S. S. Makgato, *Results Eng.*, 2023, **20**, 101521.
14 M. P. Ravele, O. C. Olatunde, O. A. Oyewo, D. C. Onwudiwe, S. S. Makgato and A. Hosseini-Bandegharaei, *Discov. Chem.*, 2025, **2**, 303.
15 X. Wang, Q. Z. Li, Y. Zhao and X. Gao, *ACS Appl. Mater. Interfaces*, 2025, **17**(49), 66110–66150, DOI: 10.1021/acsami.5c15196.

16 P. Borah, D. J. Baruah, R. Duarah and M. R. Das, *Chem. Commun.*, 2025, **61**(58), 10685–10715, DOI: 10.1039/D5CC00180C.
17 O. A. Oyewo and S. S. Makgato, *J*, 2023, **6**, 564–578.
18 P. Li, Y. Li, M. Qi and X. Zhang, *Chem. Eng. J.*, 2024, **493**, 152686, DOI: 10.1016/j.cej.2024.152686.
19 Z. Wen, J. Ke, J. Xu, S. Guo, Y. Zhang and R. Chen, *Chem. Eng. J.*, 2018, **343**, 416–426, DOI: 10.1016/j.cej.2018.03.034.
20 C. Wang, M. Huang, W. Lou, W. Xiang, T. Zhou, J. Mao, F. Zan and X. Wu, *Chem. Eng. J.*, 2022, **434**, 134575, DOI: 10.1016/j.cej.2022.134575.
21 Z. Zhao, H. An, J. Lin, M. Feng, V. Murugadoss, T. Ding, H. Liu, Q. Shao, X. Mai, N. Wang and H. Gu, *Chem. Rec.*, 2019, **19**, 873–882, DOI: 10.1002/tcr.201800153.
22 M. Rashid, D. Mowla, F. Esmaeilzadeh, K. Dashtian and M. Bahmani, *J. Clean. Prod.*, 2021, **317**, 128471, DOI: 10.1016/j.jclepro.2021.128471.
23 H. Lee, Y. Park, K. Song and J. Y. Park, *Acc. Chem. Res.*, 2022, **55**, 3727–3737, DOI: 10.1021/acs.accounts.2c00623.
24 S. Li, J. Yang, X. Ruan, X. Cui and S. K. Ravi, *Adv. Funct. Mater.*, 2026, **36**, 2503186, DOI: 10.1002/adfm.202503186.
25 P. Babu, H. Park and J. Y. Park, *J. Surf. Sci. Technol.*, 2023, **1**(1), 29, DOI: 10.1007/s44251-023-00026-1.
26 P. Babu and B. Naik, *Inorg. Chem.*, 2020, **59**, 10824–10834, DOI: 10.1021/acs.inorgchem.0c01325.
27 U. P. Gawai, S. D. Kamble, S. K. Gurav, M. N. Singh, A. K. Yadav, S. N. Jha, N. P. Lalla, M. R. Bodke, M. D. Shirsat and B. Dole, *ACS Omega*, 2022, **7**, 6700–6709, DOI: 10.1021/acsomega.1c06179.
28 P. Babu, S. Mohanty, B. Naik and K. Parida, *ACS Appl. Energy Mater.*, 2018, **1**(11), 5936–5947.
29 P. Babu, S. Mohanty, B. Naik and K. Parida, *Inorg. Chem.*, 2019, **58**(18), 12480–12491.
30 J. Li, X. Zhao, J. Liu, L. Zhang and C. Yang, *J. Alloys Compd.*, 2019, **777**, 954–962, DOI: 10.1016/j.jallcom.2018.10.204.
31 A. Manalu, K. Tarigan, S. Humaidi, M. Ginting, K. Sebayang, M. Rianna, M. Hamid, A. Subhan, P. Sebayang and I. P. Manalu, *Int. J. Electrochem. Sci.*, 2022, **17**(3), 22036, DOI: 10.20964/2022.03.11.
32 Y. Hou, C. Hou, Y. Zhai, H. Li, T. Chen, Y. Fan, H. Wang and W. Wang, *Electrochim. Acta*, 2019, **324**, 134884, DOI: 10.1016/j.seppur.2025.132072.
33 D. Pradhan, P. K. Panda, A. Mishra, E. Falletta and S. K. Dash, *Environ. Qual. Manag.*, 2022, **32**(2), 85–100, DOI: 10.1002/tqem.21916.
34 J. Oliva, C. Gomez-Solis, L. A. Diaz-Torres, A. Martinez-Luevanos, A. I. Martinez and E. Coutiño-Gonzalez, *J. Phys. Chem. C*, 2018, **122**(3), 1477–1485, DOI: 10.1021/acs.jpcc.7b10375.
35 F. T. L. Muniz, M. R. Miranda, C. Morilla dos Santos and J. M. Sasaki, *Acta Crystallogr., Sect. A: Found. Crystallogr.*, 2016, **72**, 385–390, DOI: 10.1107/S205327331600365X.
36 P. Babu, S. Mohanty, B. Naik and K. Parida, *ACS Appl. Energy Mater.*, 2018, **1**, 5936–5947.
37 P. Babu, S. Mohanty, B. Naik and K. Parida, *Inorg. Chem.*, 2019, **58**, 12480–12491.
38 N. Hoque, S. Lee, Y. B. Park, S. Roy, M. J. Baruah, S. Biswas, G. Gogoi, T. J. Bora, R. Dutta and K. K. Bania, *ChemNanoMat*, 2022, **8**(10), e202200280, DOI: 10.1002/cnma.202200280.
39 N. Hoque, M. J. Baruah, A. H. Biman, S. Biswas, G. Gogoi, R. Dutta and K. K. Bania, *ACS Appl. Energy Mater.*, 2022, **5**, 6118–6128, DOI: 10.1021/acsaem.2c00523.
40 M. J. Baruah, T. J. Bora, G. Gogoi, N. Hoque, N. K. Gour, S. K. Bhargava, A. K. Guha, J. K. Nath, B. Das and K. K. Bania, *J. Colloid Interface Sci.*, 2022, **608**, 1526–1542, DOI: 10.1016/j.jcis.2021.10.091.
41 C. Zhao, M. Li, H. Guo, X. Tong, W. Gao and C. Zhao, *J. Energy Storage*, 2024, **84**, 110950.
42 T. J. Frankcombe and Y. Liu, *Chem. Mater.*, 2023, **35**(14), 5468–5474.
43 L. A. Marquez and H. B. Dunford, *Biochemistry*, 1997, **36**(31), 9349–9355, DOI: 10.1021/bi970595j.
44 A. K. Dutta, S. K. Maji, D. N. Srivastava, A. Mondal, P. Biswas and P. Paul, *ACS Appl. Mater. Interfaces*, 2012, **4**(4), 1919–1927, DOI: 10.1021/am300408r.
45 P. Borthakur, G. Darabdhara, M. R. Das, R. Boukherroub and S. Szunerits, *Sens. Actuators, B*, 2017, **244**, 684–692.
46 P. K. Boruah, G. Darabdhara, P. Borthakur, B. Le Ouay and M. R. Das, *Chem. Eng. J.*, 2023, **474**, 145797.
47 M. Li, H. Zhang, Y. Hou, X. Wang, C. Xue and W. Li, *Nanoscale Horiz.*, 2019, **5**, 202–217, DOI: 10.1039/c9nh00577c.
48 F. Jiang, Z. Zheng, Z. Xu, S. Zheng, Z. Guo and L. Chen, *J. Hazard. Mater.*, 2005, **134**, 94–103, DOI: 10.1016/j.jhazmat.2005.10.041.
49 W. Zou, Y. Tang, H. Zeng, C. Wang and Y. Wu, *J. Hazard. Mater.*, 2021, **417**, 125994, DOI: 10.1016/j.jhazmat.2021.125994.
50 J. Shen, S. Shang, X. Chen, D. Wang and Y. Cai, *Sens. Actuators, B*, 2017, **248**, 92–100, DOI: 10.1016/j.snb.2017.03.123.
51 D. Zhang, Z. Dong, X. Jiang, M. Feng, W. Li and G. Gao, *Anal. Methods*, 2013, **5**, 1669, DOI: 10.1039/c3ay26555b.
52 P. M. Carrasco, I. García, L. Yate, R. T. Zaera, G. Cabañero and H. J. Grande, *Carbon*, 2016, **109**, 658–665, DOI: 10.1016/j.carbon.2016.08.038.
53 K. Feke, M. T. Alula, H. Spende, A. Waag and P. Lemmens, *J. Cluster Sci.*, 2022, **34**, 1009–1018, DOI: 10.1007/s10876-022-02284-9.
54 Y. Cheng, P. Shen, X. Li, X. Li, K. Chu and Y. Guo, *Sens. Actuators, B*, 2022, **376**, 132979, DOI: 10.1016/j.snb.2022.132979.
55 S. Kulandaivel, W. C. Lo, C. H. Lin and Y. C. Yeh, *Anal. Chim. Acta*, 2022, **1227**, 340335, DOI: 10.1016/j.aca.2022.340335.
56 X. Guo, F. Yang, L. Jing, J. Li, Y. Li and R. Ding, *J. Hazard. Mater.*, 2022, **431**, 128621, DOI: 10.1016/j.jhazmat.2022.128621.